2014 IEEE International Conference on Robotics & Automation (ICRA)
Hong Kong Convention and Exhibition Center
May 31 - June 7, 2014. Hong Kong, China

A Preliminary Study on using a Robotically-Actuated Delivery Sheath (RADS) for Transapical Aortic Valve Implantation

Gustaaf J. Vrooijink, Tim T. M. Ellenbroek, Paul Breedveld, Jan G. Grandjean and Sarthak Misra

***Abstract*— Recent technological advancements in cardiovascular surgery such as transapical transcatheter aortic valve implantation (TA-TAVI) enabled treatment to elderly that were initially declined surgery. However, valve malpositioning during TA-TAVI have been reported in several cases. In this preliminary study, we present a novel approach in which a Robotically-Actuated Delivery Sheath (RADS) is used to potentially facilitate valve positioning. A model is developed that describes the shape and articulating tip position of the RADS. We developed a two-dimensional ultrasound tracking method that evaluates the tip position of the RADS in ultrasound images. Both modeling and ultrasound tracking are combined into an integrated system that facilitates closed-loop control of the articulating tip of the RADS. Experiments are performed in order to evaluate the tracking accuracy of the RADS. Experiments show mean positioning errors of approximately 2 mm along the x- and y-axes. Our study demonstrates that the RADS can potentially provide compensation for beating heart and respiratory motions during valve positioning and deployment in TA-TAVI.**

I. INTRODUCTION

Technological advancements over the last decade have provided significant improvements in existing cardiovascular procedures and have enabled treatment to high-risk patients who were initially declined surgery [1]–[5]. Valve-related diseases such as severe symptomatic aortic stenosis require treatment by open heart aortic valve replacement with cardiopulmonary bypass, which is often considered a high-risk procedure for elderly with comorbidities [3], [5], [6]. However, an alternative method for treatment of aortic stenosis is provided by transfemoral (TF) or transapical (TA) transcatheter aortic valve implantation (TAVI) [3], [7], [8]. TF- and TA-TAVI are considered complementary. The TF-approach is considered to be the first option, while the TA-approach is considered if there are contraindications to the transfemoral route such as severe calcification of the aortic arch or descending aorta and limited dimensions of iliac and femoral arteries [5], [9]. The transapical approach provides direct surgical access through the apex of the heart [7]. Complications in TA-TAVI such as prosthetic valve malpositioning have been reported [5], [8], [9]. Malpositioning could cause severe peri-prosthetic aortic regurgitation, valve embolization and occlusion of arteries which often requires conversion to surgical aortic valve replacement with cardiopulmonary bypass or a valve-in-valve procedure [10]. Therefore, the success of the procedure is closely related to accurate valve orientation, positioning and deployment.

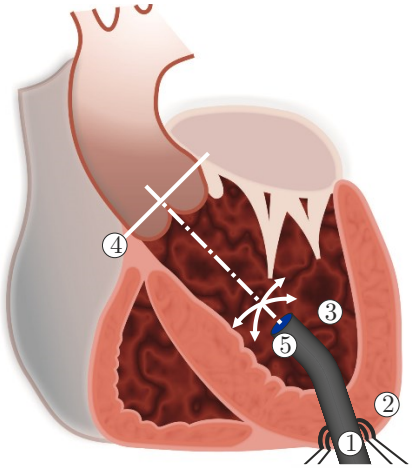

Fig. 1. Transapical transcatheter aortic valve implantation can be performed using a robotically-actuated delivery sheath (RADS) to improve valve positioning. The RADS ① is inserted through the apex ② into the left ventricle ③ and oriented perpendicular to the aortic annulus ④ for co-axial alignment. The articulating tip ⑤ of the RADS can be controlled inside the left ventricle under ultrasound image-guidance in two degrees-of-freedom by two pairs of antagonistically-configured tension wires. This enables manipulation of a catheter inside the RADS, and can potentially compensate for beating heart and respiratory motions during surgery.

Integration of robotic devices in TAVI can provide accurate valve positioning and compensation for beating heart and respiration motions to improve outcome of the procedure, and to reduce risks. A commercially-available robotic catheter, Artisan® Control Catheter (Hansen Medical, Mountain View, CA) has been reported to treat people for atrial fibrillation ablation [11]. Further, Jayender and Patel developed an actuated catheter system, and demonstrated navigation through the vascular system with potential applications in angioplasty and atrial fibrillation ablation [12]. However, neither of these systems have demonstrated applicability for TAVI-related procedures. Li *et al*. described a robotic system capable of TA-TAVI under magnetic resonance imaging (MRI) [13], [14]. But MR-imaging does not allow visualization of the existing catheters used in TAVI-related procedures without the use of markers. Another study by Kesner *et al*. demonstrated an actuated catheter system capable of tracking fast moving cardiac tissue using three-dimensional

G. J. Vrooijink, T. T. M. Ellenbroek and S. Misra are affiliated with MIRA-Institute for Biomedicial Engineering and Technical Medicine (Robotics and Mechatronics), University of Twente, The Netherlands. P. Breedveld is affiliated with the Department of BioMechanical Engineering, Delft University of Technology, The Netherlands. J. G. Grandjean is affiliated with the Department of Cardiothoracic Surgery, Thorax Center Twente, and also with MIRA-Institute for Biomedicial Engineering and Technical Medicine (Biomechanical Engineering), University of Twente, The Netherlands. The authors would like to acknowledge the help of R. J. Roesthuis (University of Twente) and J. Scheltes (DEAM Corporation, The Netherlands). This research is supported by the Dutch Technology Foundation STW (*i*MIT-Instruments for Minimally Invasive Techniques Interactive Multi-Interventional Tools (Project: MULTI)), which is part of the Netherlands Organisation for Scientific Research (NWO) and partly funded by the Ministry of Economic Affairs, Agriculture and Innovation.

(3D) ultrasound [15]. However, tracking was limited to one degree-of-freedom (DOF) in that study. Vasilyev *et al.* demonstrated a percutaneous steerable robotic tool delivery platform using pre-bent concentric tubes robot to treat patent foramen ovale [16]. Although the pre-bent concentric tubes robot could be adapted for valve delivery using transapical access, the design provides limited capabilities to compensate for respiratory and beating heart motions.

As an alternative to robotic catheters, a robotically-actuated delivery sheath (RADS) allows existing TAVI catheters to be manipulated such that valve positioning can be provided (Fig. 1). The articulating tip of the RADS can be controlled in two DOF. This allows for co-axial alignment between the prosthetic valve and the aortic annulus. Another important feature that can be provided is compensation for beating heart and respiratory motions during valve deployment. The goal of our study is to describe an integrated system that contains the modeling and ultrasound-guided control of the RADS.

A. Related work

Our work builds on two main areas of research: Modeling of continuum-type surgical robotic instruments and ultrasound tracking. Modeling is a key aspect which describes the RADS shape and articulating tip position. Modeling of continuum-type robots have been investigated by several groups [17]–[22]. Various continuum-type robotic instruments have been described in literature. These can be broadly classified into tendon-driven manipulators and pre-bent concentric tubes. In our study, we describe the kinematics of the tendon-driven constant-curvature RADS using a robot-specific and -independent submapping [18]. Another important aspect, is tracking of the RADS which provides feedback for closed-loop control. In TAVI, the surgeon is often assisted by 2D and 3D Transesophageal echocardiography or Transthoracic echocardiography [7]. 2D and 3D tracking methods of flexible instruments using 2D ultrasound have been reported [23]–[26]. Further, 3D ultrasound-based tracking of cardiac catheters (some accommodated with markers) have also been investigated [27], [28]. We focus on tracking using 2D ultrasound images, which we intend to expand to 3D ultrasound in future studies.

B. Contributions

Our preliminary study describes and demonstrates that the RADS can be potentially used to assist the surgeon in accurate valve positioning within the aortic annulus (Fig. 1). This paper focuses on robotically-assisted TA-TAVI to treat aortic stenosis, but could potentially be applied in other applications in cardiovascular surgery. A model that describes the RADS shape and tip position is used to accuratly control its articulating tip. We also develop a 2D ultrasound tracking method to provide tip feedback of the RADS. We combined ultrasound tracking with RADS modeling in order to provide model-based closed-loop control. This novel integrated system facilitates articulating tip positioning of the RADS under ultrasound closed-loop control. We evaluate the accuracy of the integrated system via closed-loop tracking experiments, in which we track various trajectories.

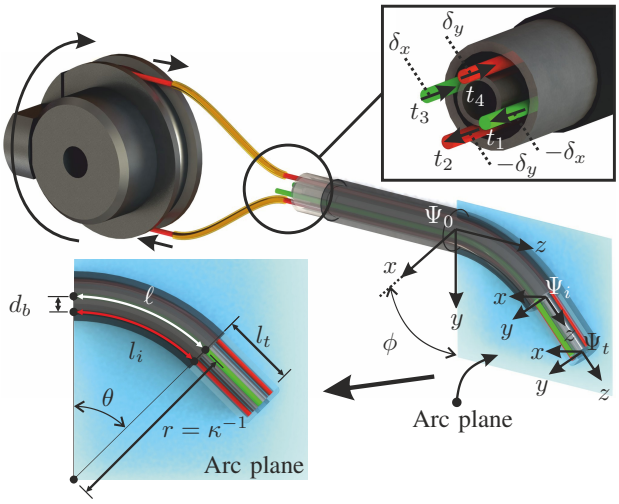

Fig. 2. An overview of the antagonistically-configured and pulley-driven robotically-actuated delivery sheath (RADS). The articulating tip of the RADS is actuated in two degrees-of-freedom by two pairs (red and green) of antagonistic-configured tension wires driven by a two pulleys (only one illustrated). The various coordinate systems are used in modeling to evaluate the tip pose of the RADS. The reference frame (Ψ_0) is fixed to the shaft of the RADS, while an intermediate frame (Ψ_i) is assigned to arc section of the RADS. Frame (Ψ_t) is fixed to the articulating tip of the RADS. The arc of the RADS lies in the plane described by the arc plane. The angle (ϕ) is used to describe the orientation of the arc plane with respect to the x-axis of the reference frame (Ψ_0). The inset (bottom-left) shows the arc-related parameters, such as arc backbone length (ℓ), arc radius (r), and curvature (κ). Further, the bend angle and tendon distance to the backbone arc (ℓ) are denoted θ and d_b, respectively. A rigid link (not completely shown) of length (l_t) is attached to the arc (frame (Ψ_i)) of the RADS. A second inset (top-right) shows the tension wires ($t_1, \cdots, t_4$) displacements δ_x and δ_y along the x- and y-axes (frame (Ψ_0)), respectively.

II. METHODS

This section explains the methods to enable closed-loop model-based control of the RADS under ultrasound image-guidance. First we describe device modeling of the RADS. Subsequently, we provide a method to track the RADS in 2D ultrasound images. Finally, we elaborate our control strategy to facilitate closed-loop control.

A. Device modeling

The design of the tendon-driven RADS used to manipulate a catheter is shown in Fig. 2. The articulating tip of the RADS is actuated in two DOF by two pairs of antagonistically-configured tension wires. Each pair of tension wires is actuated by a single pulley. This alows tip movement in 2D by using two actuators instead of three, that are required in a device with three tension wires. A general model of a tendon-driven continuum-type robot can be described by two mappings [18]. The first mapping which is often referred to as the robot-specific mapping, maps the actuator-space onto the configuration-space. The actuator-space is described by the angles of the pulleys (ψ_x and ψ_y), while the configuration-space is described by arc parameters curvature (κ), arc plane angle (ϕ) and arc length (ℓ). The second mapping (robot-independent mapping) transforms the

arc parameters (κ, ϕ and ℓ) of the configuration-space to the task space (intermediate frame (Ψ_i)).

In order to evaluate the arc parameters of the configuration-space, the relation between tendon manipulation at the base and the resulting arc needs to be described. In the derivation presented, we denote, $c_* = \cos(*)$ and $s_* = \sin(*)$, for notational simplicity. Our RADS is actuated using four tendons (t_i), where ($i = 1, \cdots, 4$) with corresponding tendon lengths (l_i) (Fig. 2). From Webster and Jones we obtain the relationship between the arc length of the RADS (ℓ) and the arc length of a single tendon (l_i) by [18]

$$\ell = l_i + \theta d_b \cos\phi_i. \tag{1}$$

In (1), θ describes the bend angle, which is related to the curvature according to $\theta = \kappa\ell$. The d_b denotes the distance between the backbone and the individual tendon, as depicted in Fig. 2. Note, that the distance (d_b) in our device is equal for all tendons. Further, ϕ_i describes the angle between the bending direction of the RADS and the location of a single tendon (t_i). Given the configuration of the tendons as illustrated in Fig. 2, we can describe the individual tendon angles by $c_{\phi_1} = c_\phi$, $c_{\phi_2} = s_\phi$, $c_{\phi_3} = -c_\phi$ and $c_{\phi_4} = -s_\phi$. This can be combined with (1) for each actuator to obtain an expression between the arc length (ℓ) of the RADS and the individual tendon lengths (l_i)

$$\ell = \frac{l_1 + l_2 + l_3 + l_4}{4}. \tag{2}$$

By combining tendon pairs (t_1 and t_3, and t_2 and t_4) which are antagonistically-configured with (2), the arc plane angle (ϕ) is given by [18]

$$\phi = \arctan\left(\frac{l_4 - l_2}{l_3 - l_1}\right), \tag{3}$$

and the curvature is evaluated as

$$\kappa = \frac{(l_1 - 3l_2 + l_3 + l_4)\sqrt{(l_4 - l_2)^2 + (l_3 - l_1)^2)}}{d_b(l_1 + l_2 + l_3 + l_4)(l_4 - l_2)}. \tag{4}$$

Note, that the tendon lengths (l_i) are manipulated by displacements (δ_x) and (δ_y) (Fig. 2). These displacements are provided by two actuated pulleys, and can be rewrite as tendon displacements as functions of pulley angles according to $\delta_x = r_p\psi_x$ and $\delta_y = r_p\psi_y$, where r_p describe the pulley radius (equal radii for both pulleys), and ψ_x and ψ_y denote the pulley angles, respectively. Hence, we can use (1) to describe each tendon manipulation as a function of the pulley angles (ψ_x and ψ_y) by $l_1 = \ell - r_p\psi_x$, $l_2 = \ell - r_p\psi_y$, $l_3 = \ell + r_p\psi_x$, and $l_4 = \ell + r_p\psi_y$. Substituting this into (3) and (4) yields

$$\phi = \arctan\left(\frac{\psi_y}{\psi_x}\right), \tag{5}$$

and

$$\kappa = \frac{r_p\sqrt{\psi_x^2 + \psi_y^2}}{\ell d_b}. \tag{6}$$

Thus, we obtain the arc parameters (κ, ϕ and ℓ) of the configuration-space as a function of the pulley angles (ψ_x and ψ_y).

The independent-mapping is given by the homogeneous transformation matrix ($\mathbf{H}_i^0$) [18]

$$\mathbf{H}_i^0 = \begin{bmatrix} c_\phi c_{\kappa\ell} & -s_\phi & c_\phi s_{\kappa\ell} & \frac{c_\phi(1-c_{\kappa\ell})}{\kappa} \\ s_\phi c_{\kappa\ell} & c_\phi & s_\phi s_{\kappa\ell} & \frac{s_\phi(1-c_{\kappa\ell})}{\kappa} \\ -s_{\kappa\ell} & 0 & c_{\kappa\ell} & \frac{s_{\kappa\ell}}{\kappa} \\ 0 & 0 & 0 & 1 \end{bmatrix}, \tag{7}$$

which expresses the intermediate frame (Ψ_i) with respect to the reference frame (Ψ_0). However, we attached a rigid link to the arc section (intermediate frame (Ψ_i)) of the RADS. Hence, we describe the articulating tip frame (Ψ_t) of the RADS with respect to the intermediate frame (Ψ_i) by transformation matrix ($\mathbf{H}_t^i$)

$$\mathbf{H}_t^i = \begin{bmatrix} \mathbf{I}_3 & \mathbf{L}_t^i \\ \mathbf{0}_3^T & 1 \end{bmatrix}, \tag{8}$$

where $\mathbf{I}_3$ denotes a 3x3 identity matrix and $\mathbf{L}_t^i = [0\ 0\ l_t]^T$ represents a translation along the z-axis of the intermediate frame (Ψ_i). The subsequent multiplications of homogeneous transformation matrices ($\mathbf{H}_i^0$ and $\mathbf{H}_t^i$) describe the RADS articulating tip pose expressed in the reference frame (Ψ_0).

In order to control the articulating tip to a reference position ($\mathbf{r}_t^0 \in \mathbb{R}^{4\times1}$, where $\mathbf{r}_t^0 = [r_x\ r_y\ r_z\ 1]^T$), the inverse kinematics of the RADS are required. The inverse kinematics are used to express the pulley angles (ψ_x and ψ_y) as a function of the referenced tip position ($\mathbf{r}_t^0$). The reference position ($\mathbf{r}_t^0$) can be used to determine the arc parameters of the configuration-space. We first evaluate the arc plane angle (ϕ) according to

$$\phi = \arctan\left(\frac{r_y}{r_x}\right). \tag{9}$$

Subsequently, we obtain an expression for the reference position ($\mathbf{r}_t^0$) by using the forward kinematics of (7) and (8) according to $\mathbf{r}_t^0 = \mathbf{H}_i^0\mathbf{H}_t^i\mathbf{o}_t$, where $\mathbf{o}_t \in \mathbb{R}^{4\times1}$ ($\mathbf{o}_t = [0\ 0\ 0\ 1]^T$) describes the origin of the articulating tip frame (Ψ_t), which yields

$$\mathbf{r}_t^0 = \begin{bmatrix} c_\phi\left(\frac{(1-c_{\kappa\ell})}{\kappa} + l_t c_{\kappa\ell}\right) \\ s_\phi\left(\frac{(1-c_{\kappa\ell})}{\kappa} + l_t c_{\kappa\ell}\right) \\ \frac{s_{\kappa\ell}}{\kappa} + l_t c_{\kappa\ell} \\ 1 \end{bmatrix}. \tag{10}$$

By substituting (9) into (10), we can numerically solve for the curvature (κ). The evaluated curvature (κ) and arc plane angle (ϕ) from (9) can be used to solve (1) for all individual tendon lengths (l_i). Note, that the individual tendon lengths are manipulated by the pulley angles (ψ_x and ψ_y), thus known.

B. Ultrasound tracking of actuated delivery sheath

This section describes the ultrasound image segmentation applied to evaluate the centroid location of the RADS in 2D ultrasound images. The ultrasound transducer is placed at the tip of the RADS and orientated perpendicular to its shaft in order to display the radial cross-sectional view of

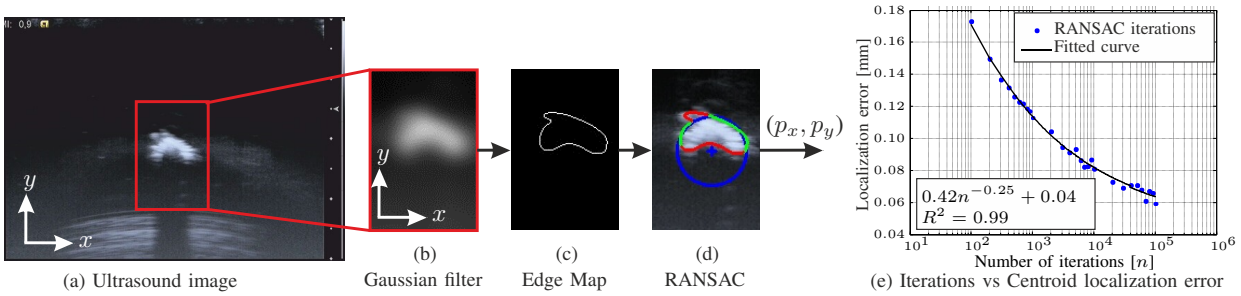

(a) Ultrasound image (e) Iterations vs Centroid localization error

Fig. 3. Image processing technique to determine the centroid location (p_x,p_y) of the robotically-actuated delivery sheath (RADS) in the ultrasound images. (a) The ultrasound input image is a radial cross-sectional view of the RADS. (b) Filtering using a two-dimensional Gaussian kernel. (c) Canny edge detection with hysteresis thresholding. (d) Random sample consensus (RANSAC) is used to evaluate the centroid location (p_x,p_y) of the RADS (center of the blue circle). The green and red points are considered inliers and outliers, respectively. (e) The relation between the number iterations and the localization error is evaluated using a sequence of 600 ultrasound images with a ground truth measurement obtained after 10^6 iterations.

the RADS (Fig. 3). A representative ultrasound image of the RADS submerged in a water container is shown in Fig. 3(a). The ultrasound images show the semi-circular shape which describes the surface reflection of the RADS. A semi-circular shape with identical radius is not found within anatomical structures of the beating heart. This allows for segmentation of RADS based on circular shape parameters. Further, the contrast between device and the environment is sufficiently large for edge detection.

Before edge detection can be applied, we use a 2D Gaussian kernel to reduce speckle and to smoothen edges in the ultrasound image (Fig. 3(b)). A Canny edge detector with hysteresis thresholding is used to evaluate an edge map of the ultrasound image (Fig. 3(c)) [29]. Hysteresis thresholding is used to reduce detection of irrelevant edges, which do not describe the surface the RADS. However, surface deformations by artifacts and bending of the device, or irrelevant edges may still be present. Hence, the centroid location is evaluated using a random sample consensus (RANSAC) algorithm (Algorithm. 1) that is robust to deformations and irrelevant edges that do not describe the surface of the RADS [29].

The set (A) of edge points ($\mathbf{x}$) are evaluated from the Canny edge detector and provided as an input to the RANSAC algorithm. The algebraic circle model parameters (m) are fitted ($f : H \rightarrow m$) to a set (H) of three randomly selected (from A) candidate inliers. A preliminary test $\big(suffice(m_k)\big)$ is performed to determine if the evaluated model parameters such as radius and location are consistent with those of the RADS. Subsequently, we use a cost function $\big(C(m, \mathbf{x})\big)$ to evaluate all data points of the edge map against the fitted model (i.e., sufficiently close to the periphery of the circular shape). The fitted model is acceptable if a sufficiently large portion of the surface (semi-circle) has been evaluated as the consensus set. The model parameters and consensus set are both refined if the computed cost (J_k) of the current iteration is larger than the previous best cost evaluated from a preceding iteration. The localization accuracy of the RADS increases if the number (n) of iterations of the RANSAC algorithm are increased. We empirically determine the relation between the number of iterations and the localization error using a ground truth measurement obtained after 10^6 iterations (Fig 3(e)). After n iterations are completed, the best consensus set is used to re-

Algorithm 1 Random sample consensus device localization

Inputs:

$A \leftarrow \{\mathbf{x}_{v|v=1,\cdots,w}\}$ ▷ Set of detected edge points ($\mathbf{x}$)

$f : H \rightarrow m$ ▷ Computes the algebraic circle model parameters (m) from a set (H) of three randomly selected data points

$C(m, \mathbf{x})$ ▷ Cost function for a single data point (1 if $\mathbf{x}$ is an inlier to the algebraic circle parameters (m), 0 otherwise)

n ▷ Number of iterations

Outputs:

m^* ▷ Best model parameters

S^* ▷ Best consensus set (inliers)

J^* ▷ Best cost

Method:

for $k \leftarrow 1, n$ **do**
  $H_k \leftarrow random\_3pnts(A)$ ▷ (I) Hypothesis
  $m_k \leftarrow f(H_k)$
  if $suffice(m_k)$ **then** ▷ (II) Preliminary test
    $S_k \leftarrow \{\forall \mathbf{x} \in A | C(m_k, \mathbf{x}) = 1\}$
    $J_k \leftarrow \sum_{\mathbf{x} \in A} C(m_k, \mathbf{x})$
    if $J^* < J_k$ **then** ▷ (III) Evaluation
      $J^* \leftarrow J_k$
      $m^* \leftarrow m_k$
      $S^* \leftarrow S_k$
    end if
  end if
  $k \leftarrow k + 1$
end for

estimate the model parameters using a least squares algebraic circle fit [29]. The centroid location (p_x, p_y) of RADS is evaluated from the model parameters (m) and displayed as the center of the circle (Fig. 3(d)).

C. Ultrasound-guided control

In this section, we describe the model-based control architecture used to control the articulating tip of the RADS (Fig. 4). The model integrated in the observer of the control architectures is described in Section II-A, and used to evaluate the shape and tip position of the RADS. The inverse model is used to transform the desired tip posi-

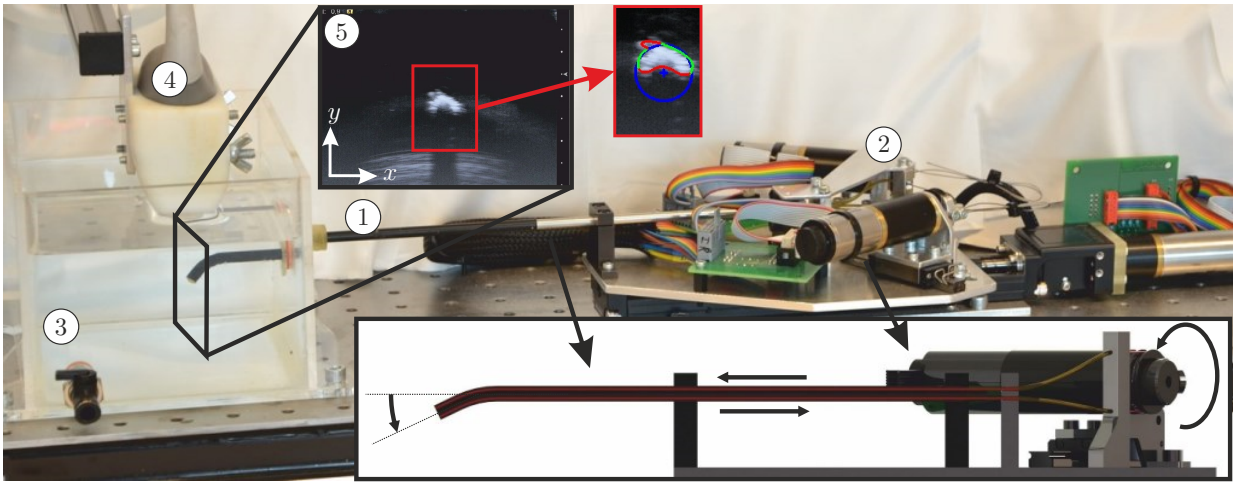

Fig. 5. The experimental setup used to control the robotically-actuated delivery sheath (RADS). ① Actuated delivery sheath. ② Motors and accompanying electronics used to control the articulating tip of the RADS. The inset depicts a longitudinal cross-section of the RADS. An antagonistic configuration of a pair of tension wires (red) is actuated by a pulley-driven system. Each pair of tension wires (total of two pairs) is guided through the flexible shaft and through two incompressible tubes (yellow) to actuate a single degree-of-freedom of the articulating tip. ③ Container filled with water. ④ Ultrasound transducer. ⑤ Ultrasound image with a radial cross-sectional view of the RADS (Fig. 3).

tion ($\mathbf{r} \in \mathbb{R}^{2\times1}$, where $\mathbf{r} = [r_x \ r_y]^T$) to pulley angles ($\boldsymbol{\psi} \in \mathbb{R}^{2\times1}$, where $\boldsymbol{\psi} = [\psi_x \ \psi_y]^T$). Subsequently, the pulley angles ($\boldsymbol{\psi}$) are provided as an input to the RADS and the Extended Kalman Filter (EKF). The tip position ($\mathbf{p} \in \mathbb{R}^{2\times1}$, where $\mathbf{p} = [p_x \ p_y]^T$) of the RADS is measured using a 2D ultrasound transducer as described in Section II-B, while an estimated tip position ($\hat{\mathbf{p}} \in \mathbb{R}^{2\times1}$, where $\hat{\mathbf{p}} = [\hat{p_x} \ \hat{p_y}]^T$) is provided by the EKF [30]. Ultrasound images are often prone to noise, and the device tip may not always be detected during tracking. Therefore, an EKF can be used to model process and measurement noise in order to provide state estimation based on both model and measurements. The position error ($\mathbf{e} \in \mathbb{R}^{2\times1}$) is obtained by $\mathbf{e} = \mathbf{p} - \hat{\mathbf{p}}$, and is used to close the loop. Further, no measurement of the RADS in the z-axis of frame (Ψ_0) is available while using 2D ultrasound. In order to limit the articulating tip motion to the 2D ultrasound image plane, positioning of the RADS along the z-axis of frame (Ψ_0) is performed by an open-loop model-based controller.

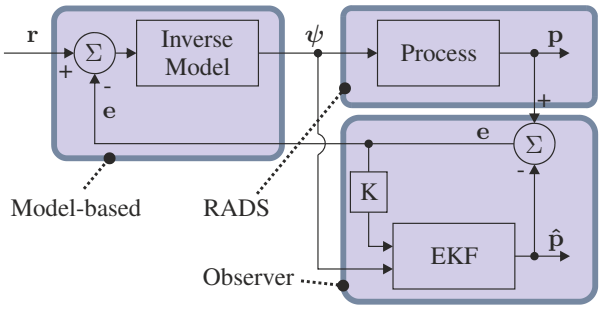

Fig. 4. The closed-loop controller used to actuate the robotically-actuated delivery sheath (RADS). The desired tip position is denoted by $\mathbf{r}$, whose actual and estimated positions are described by $\mathbf{p}$ and $\hat{\mathbf{p}}$, respectively. The pulley angle is denoted by $\boldsymbol{\psi}$ and provided as an input to the RADS and the Extended Kalman Filter (EKF). The resulting positioning error is given by $\mathbf{e}$, which is used to provide closed-loop control, and as an input to the EKF with a gain (K).

III. Experiments and Validation

This section describes the experimental evaluation of the RADS. First, we explain the experimental setup used to control the RADS. Subsequently, we describe the experiments performed in order to evaluate the performance of our RADS. Finally, we discuss our experimental results.

A. Experimental Setup

The experimental setup used to control the articulating tip of the RADS is shown in Fig. 5. The design of the actuated delivery sheath is based on a cable-ring structure surrounded by a hinged-tube (DEAM Corporation, Amsterdam, The Netherlands) [31]. The device has a diameter of 5 mm, a backbone arc length (ℓ) of 15 mm and a rigid link length (l_t) of 8 mm. Further, for all tension wires, the distance between the backbone and the tension wire (d_b) equals 1.85 mm. The articulating tip of the RADS is actuated using two pairs of tension wires which provide tip movement in two DOF. Each pair of tension wires is antagonistically-configured (inset of Fig. 5) and controlled by a pulley with radius ($r_p = 9.3$ mm) which is driven by an ECMax22 motor with a GP32/22 gearhead (Maxon Motor, Sachseln, Switzerland). The complete system is mounted on a LX30 translational stage (Misumi Group Inc., Tokyo, Japan) which can be translated along the longitudinal axis of the delivery sheath. All motors are controlled in position by an Elmo Whistle 2.5/60 motor controller (Elmo Motion Control Ltd, Petach-Tikva, Israel). The tip of the RADS is inserted though a sealed plug into a container filled with water which is used to visualize the device using ultrasound images. In order to provided feedback of the articulating tip as described in Section II-B, ultrasound images are obtained by an 18 MHz transducer (18L6) on a Siemens Acuson S2000™ ultrasound system (Siemens AG, Erlangen, Germany). We position the ultrasound transducer over the articulating tip of the RADS, while we acquire images with a

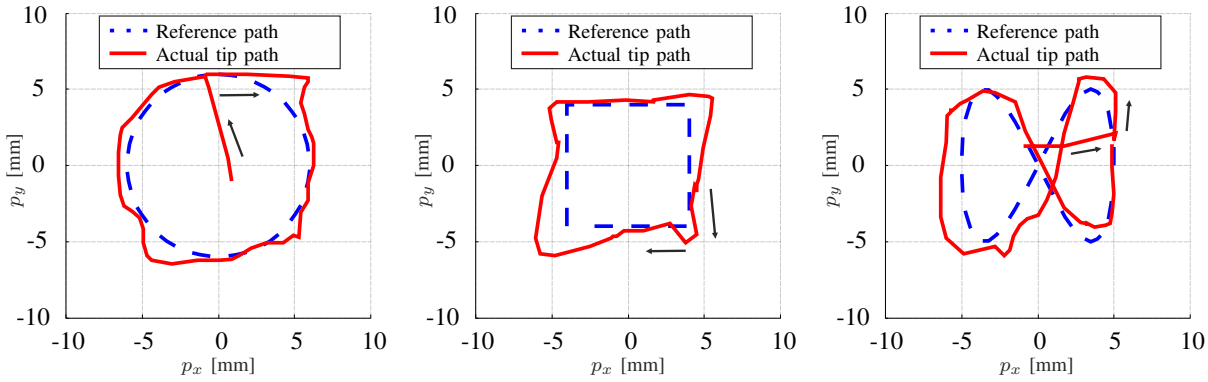

(a) Circle (b) Square (c) Figure-eight

Fig. 6. Representative experimental closed-loop control results of the articulating tip ($\mathbf{p} \in \mathbb{R}^{2\times 1}$, where $\mathbf{p} = [p_x \ p_y]^T$) of the robotically-actuated delivery sheath during tracking of circular, square and figure-eight paths. The blue dashed line trajectory represents the reference path, while the red line represents the actual path taken by the articulating tip. ***Please refer to the accompanying video that demonstrates the results of real-time tip tracking.***

frequency of 16 MHz, a power level of -4 dB and a scanning depth of 4 cm. This results in an effective in-plane resolution of approximately 0.12 mm per pixel. The S-video output of the ultrasound machine is used to transfer the images to a computer (2.80 GHz Intel® I7, 8-GB internal memory and 64-bit Windows 7) with a frame rate of 25 frames per second. Compensation for out-of-image-plane motion of the articulating tip is provided by positioning the RADS along the longitudinal axis.

B. Experimental Plan

A series of experiments have been conducted in order to evaluate the performance of the integrated system. The RADS was controlled along various paths under closed-loop control using ultrasound images. We evaluate closed-loop control of the articulating tip of the RADS during tracking of circular, square and figure-eight paths (Fig. 6). The circle has a radius of 6 mm, while the sides of the square are 8 mm and the amplitudes of the figure-eight are 5 mm along the x- and y-axes. All trajectories were evaluated using an articulating tip velocity of 2.0 mm/s.

C. Experimental Results

The results of the experiments described in the experimental plan are reported in Table I, while a single representative of each experiment can be found in Fig. 6. The experiments were repeated five times in order to evaluate the tracking performance of the RADS. Experiments show mean positioning errors of 1.90 mm and 2.28 mm along the x- and y-axes, respectively, while the RANSAC algorithm completes on average 599 iterations (single CPU core implementation).

In the circular path experiments we observe a shape slightly bigger than the reference path. Similar results are also observed in the square and figure-eight paths. This could be the result of measurement delay in the closed-loop control system. We use a capturing device to obtain 2D ultrasound images from the ultrasound system, which could potentially introduce a delay in the closed-loop controller. Further, we observe several peaks, especially when the motion of a tendon pair changes sign. This could be explained by mechanical hysteresis in the RADS or its actuators. However, it can not be ruled out that some of these effects could be due to tendon elongation or crosstalk between the two tendon pairs (i.e., displacement in one tendon pair influences the other tendon pair).

IV. Conclusions and Future Work

This preliminary study presents a novel approach in which the RADS is used to potentially manipulate existing catheters in TA-TAVI-related procedures in order to facilitate valve positioning. A model is derived to describe the RADS shape and articulating tip position, which is integrated in a model-based control architecture. We developed a 2D ultrasound tracking method to evaluate the position of the RADS in ultrasound images. This results in an integrated system capable of controlling the articulating tip of the RADS in closed-loop manner by using ultrasound images and an EKF. We experimentally evaluate the closed-loop control performance of the RADS. Experiments show mean positioning errors of approximately 2 mm along the x- and y-axes.

In future work, we intend to address the problems introduced by delay and hysteresis. Performance can be improved by reducing the delay in the system, and providing compensation for mechanical hysteresis. Further, predictive control can provide a solution to delay, especially during tracking of motions that are fast and periodic such as beating

TABLE I

Experimental closed-loop control results of the robotically-actuated delivery sheath tip tracking for circular, square and figure-eight paths. The root mean square position errors (ϵ_x and ϵ_y) with standard deviation (five experiments) are reported along the x- and y-axes, respectively. ***Please refer to the accompanying video that demonstrates the results of real-time tip tracking.***

Case	ϵ_x [mm]	ϵ_y [mm]
Circle	1.90±0.02	2.28±0.09
Square	1.87±0.12	2.04±0.36
Figure-eight	1.52±0.13	1.93±0.02

heart and respiratory motions. We also intend to integrate 3D ultrasound in our system in which both tissue and instrument motions are tracked. Additionally, optical shape sensing and electromagnetic tracking sensors can be beneficial to provide instrument information. Further, we plan to include a realistic circulatory cardiac environment in our setup which uses a heart pump and a biological aortic valve. Nonetheless, our current system demonstrates that the RADS can be controlled under ultrasound image-guidance by a model-based closed-loop control architecture. This could potentially enable manipulation of existing catheters in order to provide accurate valve positioning.

REFERENCES

[1] A. Cribier, H. Eltchaninoff, C. Tron, F. Bauer, C. Agatiello, L. Sebagh, A. Bash, D. Nusimovici, P. Litzler, J.-P. Bessou, and M. B. Leon, "Early experience with percutaneous transcatheter implantation of heart valve prosthesis for the treatment of end-stage inoperable patients with calcific aortic stenosis," *Journal of the American College of Cardiology*, vol. 43, no. 4, pp. 698–703, 2004.

[2] O. Alfieri, M. D. Bonis, F. Maisano, and G. L. Canna, "Future directions in degenerative mitral valve repair," *Seminars in Thoracic and Cardiovascular Surgery*, vol. 19, no. 2, pp. 127–132, 2007.

[3] D. Himbert, F. Descoutures, N. Al-Attar, B. Iung, G. Ducrocq, D. Détaint, E. Brochet, D. Messika-Zeitoun, F. Francis, H. Ibrahim, P. Nataf, and A. Vahanian, "Results of transfemoral or transapical aortic valve implantation following a uniform assessment in high-risk patients with aortic stenosis," *Journal of the American College of Cardiology*, vol. 54, no. 4, pp. 303–311, 2009.

[4] J. Seeburger, M. A. Borger, H. Tschernich, S. Leontjev, D. Holzhey, T. Noack, J. Ender, and F. W. Mohr, "Transapical beating heart mitral valve repair," *Circulation: Cardiovascular Interventions*, vol. 3, no. 6, pp. 611–612, 2010.

[5] J. Ye, A. Cheung, S. V. Lichtenstein, F. Nietlispach, S. Albugami, J.-B. Masson, C. R. Thompson, B. Munt, R. Moss, R. G. Carere, W. R. E. Jamieson, and J. G. Webb, "Transapical transcatheter aortic valve implantation: Follow-up to 3 years," *The Journal of Thoracic and Cardiovascular Surgery*, vol. 139, no. 5, pp. 1107–1113, 2010.

[6] B. Iung, A. Cachier, G. Baron, D. Messika-Zeitoun, F. Delahaye, P. Tornos, C. Gohlke-Bärwolf, E. Boersma, P. Ravaud, and A. Vahanian, "Decision-making in elderly patients with severe aortic stenosis: why are so many denied surgery?," *European Heart Journal*, vol. 26, no. 24, pp. 2714–2720, 2005.

[7] T. Walther, T. Dewey, M. A. Borger, J. Kempfert, A. Linke, R. Becht, V. Falk, G. Schuler, F. W. Mohr, and M. Mack, "Transapical aortic valve implantation: Step by step," *The Annals of Thoracic Surgery*, vol. 87, no. 1, pp. 276–283, 2009.

[8] D. R. Wong, J. Ye, A. Cheung, J. G. Webb, R. G. Carere, and S. V. Lichtenstein, "Technical considerations to avoid pitfalls during transapical aortic valve implantation," *The Journal of Thoracic and Cardiovascular Surgery*, vol. 140, no. 1, pp. 196–202, 2010.

[9] M. Johansson, S. Nozohoor, P. O. Kimblad, J. Harnek, G. K. Olivecrona, and J. Sjögren, "Transapical versus transfemoral aortic valve implantation: A comparison of survival and safety," *The Annals of Thoracic Surgery*, vol. 91, no. 1, pp. 57–63, 2011.

[10] Ê. E. Guérios, S. Gloekler, T. Pilgrim, S. Stortecky, L. Büllesfeld, A. A. Khattab, C. Huber, B. Meier, S. Windecker, and P. Wenaweser, "Second valve implantation for the treatment of a malpositioned transcatheter aortic valve," *Journal of Invasive Cardiology*, vol. 24, no. 9, pp. 457–462, 2012.

[11] W. Saliba, V. Y. Reddy, O. Wazni, J. E. Cummings, J. D. Burkhardt, M. Haissaguerre, J. Kautzner, P. Peichl, P. Neuzil, V. Schibgilla, G. Noelker, J. Brachmann, L. Di Biase, C. Barrett, P. Jais, and A. Natale, "Atrial fibrillation ablation using a robotic catheter remote control systeminitial human experience and long-term follow-up results," *Journal of the American College of Cardiology*, vol. 51, pp. 2407–2411, June 2008.

[12] J. Jayender, R. V. Patel, and S. Nikumb, "Robot-assisted active catheter insertion: Algorithms and experiments," *The International Journal of Robotics Research*, vol. 28, no. 9, pp. 1101–1117, 2009.

[13] M. Li, A. Kapoor, D. Mazilu, and K. Horvath, "Pneumatic actuated robotic assistant system for aortic valve replacement under mri guidance," *IEEE Transactions on Biomedical Engineering*, vol. 58, no. 2, pp. 443–451, 2011.

[14] M. Li, D. Mazilu, and K. A. Horvath, "Minimally invasive cardiac surgery: Transapical aortic valve replacement," *Minimally invasive surgery*, vol. 2012, p. 10, 2012.

[15] S. B. Kesner and R. D. Howe, "Force control of flexible catheter robots for beating heart surgery," in *Proceedings of the IEEE International Conference on Robotics and Automation (ICRA)*, pp. 1589–1594, Shanghai, China, May 2011.

[16] N. V. Vasilyev, A. H. Gosline, E. Butler, N. Lang, P. J. Codd, H. Yamauchi, E. N. Feins, C. R. Folk, A. L. Cohen, R. Chen, D. Zurakowski, P. J. del Nido, and P. E. Dupont, "Percutaneous steerable robotic tool delivery platform and metal microelectromechanical systems device for tissue manipulation and approximation: Closure of patent foramen ovale in an animal model.," *Circulation. Cardiovascular interventions*, vol. 6, no. 4, pp. 468–475, 2013.

[17] D. Camarillo, C. Milne, C. Carlson, M. Zinn, and J. Salisbury, "Mechanics modeling of tendon-driven continuum manipulators," *IEEE Transactions on Robotics*, vol. 24, no. 6, pp. 1262–1273, 2008.

[18] R. J. Webster III and B. A. Jones, "Design and kinematic modeling of constant curvature continuum robots: A review," *International Journal of Robotics Research*, vol. 29, no. 13, pp. 1661–1683, 2010.

[19] P. E. Dupont, J. Lock, B. Itkowitz, and E. Butler, "Design and control of concentric-tube robots," *IEEE Transactions on Robotics*, vol. 26, no. 2, pp. 209–225, 2010.

[20] J. Ding, K. Xu, R. Goldman, P. Allen, D. Fowler, and N. Simaan, "Design, simulation and evaluation of kinematic alternatives for insertable robotic effectors platforms in single port access surgery," in *Proceedings of the IEEE International Conference on Robotics and Automation (ICRA)*, pp. 1053–1058, Anchorage, USA, May 2010.

[21] B. Bardou, P. Zanne, F. Nageotte, and M. De Mathelin, "Control of a multiple sections flexible endoscopic system," in *Proceedings of the IEEE International Conference on Intelligent Robots and Systems (IROS)*, pp. 2345–2350, Taipei, Taiwan, October 2010.

[22] A. Reiter, A. Bajo, K. Iliopoulos, N. Simaan, and P. Allen, "Learning-based configuration estimation of a multi-segment continuum robot," in *Proceedings of the IEEE International Conference on Biomedical Robotics and Biomechatronics (BioRob)*, pp. 829–834, Rome, Italy, June 2012.

[23] J. Hong, T. Dohi, M. Hashizume, K. Konishi, and N. Hata, "An ultrasound-driven needle-insertion robot for percutaneous cholecystostomy," *Physics in Medicine and Biology*, vol. 49, no. 3, pp. 441–455, 2004.

[24] H. R. S. Neshat and R. V. Patel, "Real-time parametric curved needle segmentation in 3d ultrasound images," in *Proceedings of the IEEE RAS EMBS International Conference on Biomedical Robotics and Biomechatronics (BioRob)*, pp. 670–675, Scottsdale, USA, October 2008.

[25] Z. Neubach and M. Shoham, "Ultrasound-guided robot for flexible needle steering," *IEEE Transactions on Biomedical Engineering*, vol. 57, no. 4, pp. 799–805, 2010.

[26] G. J. Vrooijink, M. Abayazid, and S. Misra, "Real-time three-dimensional flexible needle tracking using two-dimensional ultrasound," in *Proceedings of the IEEE International Conference on Robotics and Automation (ICRA)*, pp. 1680–1685, Karlsruhe, Germany, May 2013.

[27] P. M. Novotny, J. A. Stoll, N. V. Vasilyev, P. J. del Nido, P. E. Dupont, T. E. Zickler, and R. D. Howe, "GPU based real-time instrument tracking with three-dimensional ultrasound," *Medical Image Analysis*, vol. 11, no. 5, pp. 458–464, 2007.

[28] J. Stoll, H. Ren, and P. Dupont, "Passive markers for tracking surgical instruments in real-time 3d ultrasound imaging," *IEEE Transactions on Medical Imaging*, vol. 31, no. 3, pp. 563–575, 2012.

[29] D. A. Forsyth and J. Ponce, *Computer vision a modern approach*. Prentice Hall, 2003.

[30] Y. Bar-Shalom, X. R. Li, and T. Kirubarajan, *Estimation with Applications to Tracking and Navigation*. New York, USA: John Wiley & Sons., 2001.

[31] P. Breedveld, "Steerable laparoscopic cable-ring forceps," in *Proceedings of the Design of Medical Devices Conference (DMD)*, p. 7, Minneapolis, MN, USA, April 2010.